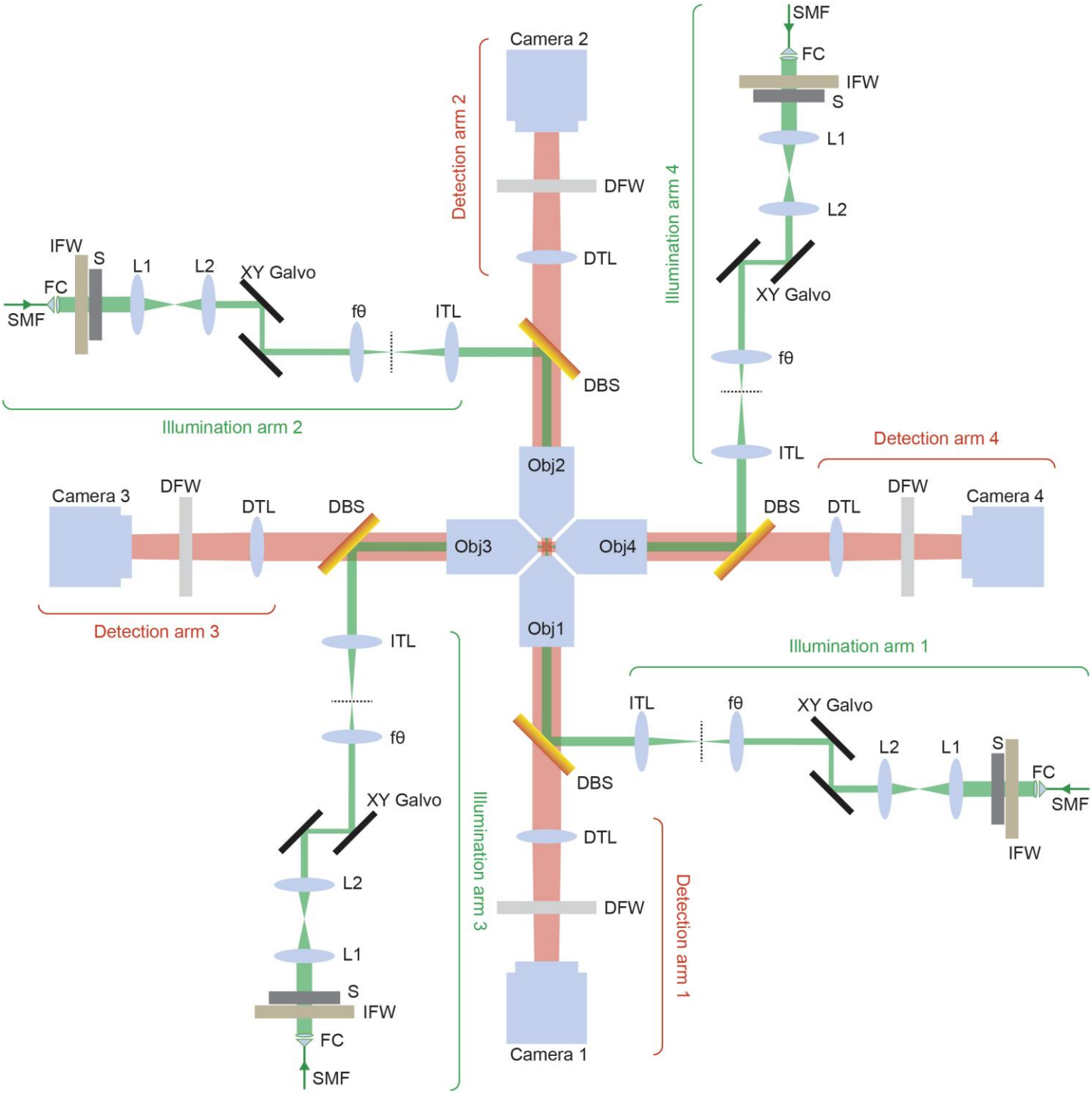


**Supplementary Figure 1**

Optical design of the IsoView light-sheet microscope.

IsoView illumination arms: Beams from multiple lasers (488 nm, 515 nm, 561 nm, 594 nm), led through single mode fibers (SMF), are collimated by fiber collimators (FC) and directed through illumination filter wheels (IFW) and shutters (S). Lens pairs (L1 and L2) de-magnify the beams to attain the intended Rayleigh length of the weakly focused beams in sample space. De-magnified beams are then scanned by dual-axis galvanometer scanners (XY Galvo) to rapidly generate scanned light sheets as well as to laterally translate light

sheets in sample space. The planar scanned fields (dotted lines) generated by the f-theta scan lenses (fθ) are reimaged onto the sample plane by the illumination tube lenses (ITL) and objectives (Obj1, Obj2, Obj3 and Obj4), via reflection from dichroic beam splitters (DBS) en route to sample space.

IsoView detection arms: The emitted fluorescence signal collected from the focal planes of the objectives orthogonal to the light sheets is transmitted by dichroic beam splitters located in infinity space between detection tube lenses (DTL) and objectives. The objectives and detection tube lenses image the fluorescent signal emitted by the specimen onto the sCMOS camera chips, following transmission through the detection filter wheels (DFW). Depth-sectioned images are acquired by linearly translating the objectives mounted atop linear piezos (not shown) and synchronously translating the light sheets laterally to match the focal planes of the objectives collecting the emitted fluorescence light.

We note that, in order to reduce the footprint of the microscope, X and Y scan mirrors in the IsoView illumination arms are not conjugated. Depending on which scan mirror is positioned in the focal plane of the f-theta lens, this arrangement is thus non-telecentric for the respective other scan direction. The implications of this design choice are briefly summarized below.

Case 1: When beam scanning is non-telecentric in the direction that sweeps the Gaussian beam over the camera field, the angle between beam and optical axis is at maximum 1.8 degrees (measured across the full field-of-view, i.e. +/- 400 µm). For a *Drosophila*-sized specimen, this amounts to a vertical beam offset of 6.3 µm at the two ends of the specimen. Since the size of the confocal slit typically used in IsoView mode 2 is 29.3 µm, the slit is large enough to collect all ballistic photons and there is in principle no impact on image quality.

Case 2: When beam scanning is non-telecentric in the direction that sweeps the light sheet across the sample volume, the angle between light sheet and focal plane is at maximum 0.8 degrees across a 400-µm-deep volume. At the end points of a 200-µm-wide volume this corresponds to a maximum shift of +/- 1.4 µm between light sheet and detection plane. For comparison, the light sheet waist is typically on the order of 6.3 µm.

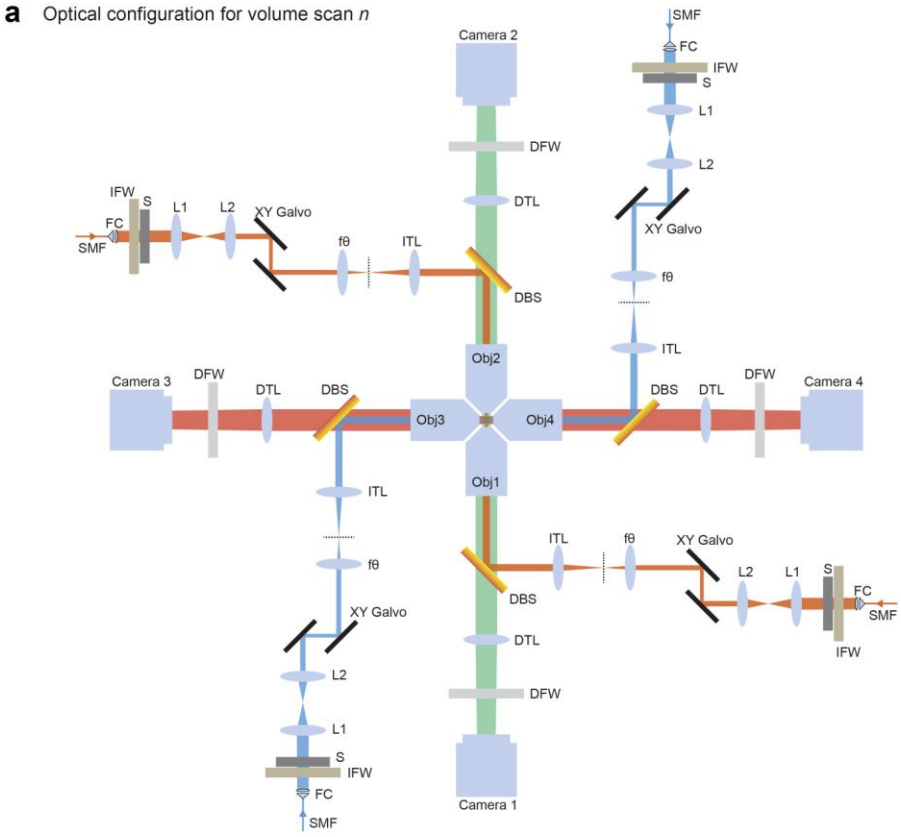
a Optical configuration for volume scan n
Camera 2
SMF
FC
IFW
S
L1
L2
XY Galvo
fθ
ITL
DFW
DTL
DBS
Obj2
Obj1
Obj3
Obj4
Camera 3
Camera 4
Camera 1

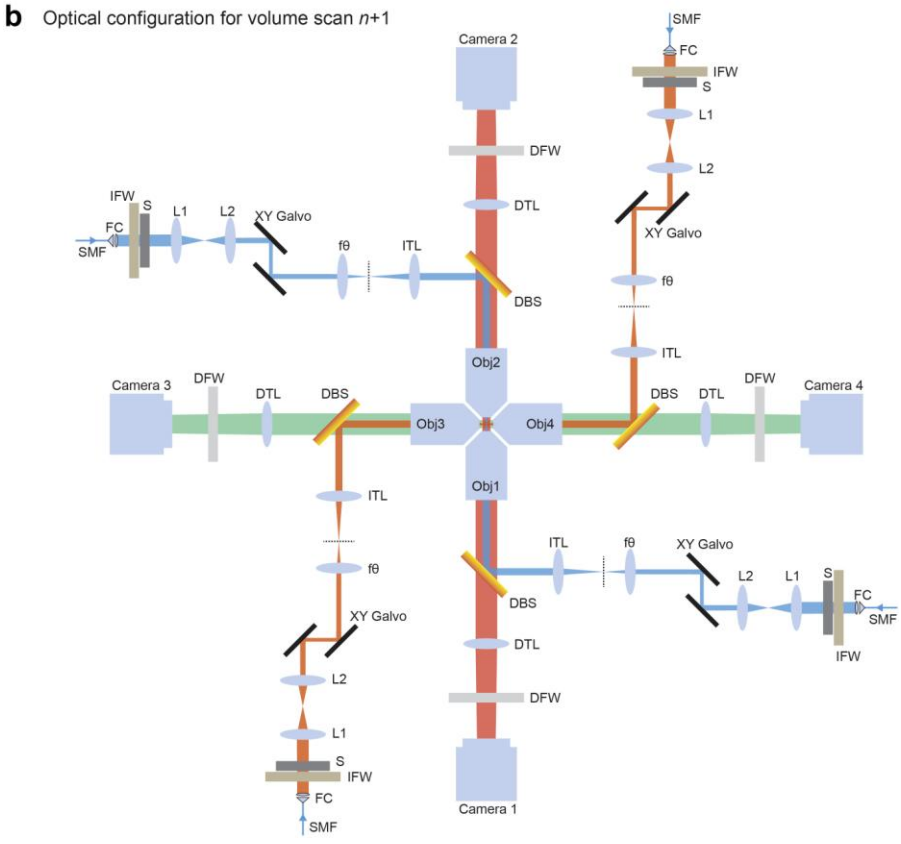
b Optical configuration for volume scan n+1
Camera 2
SMF
FC
IFW
S
L1
L2
XY Galvo
fθ
ITL
DFW
DTL
DBS
Obj2
Obj1
Obj3
Obj4
Camera 3
Camera 4
Camera 1

**Supplementary Figure 2**

IsoView two-color imaging.

IsoView schematic as shown in **Supplementary Fig. 1**, but indicating the two different wavelength configurations used for rapid four-view, two-color imaging in IsoView mode 3 (**Fig. 1d**). The microscope quickly alternates between configurations (**a**) and (**b**), in which the specimen is illuminated with two different laser wavelengths and two different spectral bands are imaged along orthogonal axes. Color assignments in the four illumination and detection arms are flipped in orthogonal arms when switching between configurations (**a**) and (**b**). Completing a full volumetric imaging cycle with both wavelength configurations produces four-view image data sets for both spectral channels.

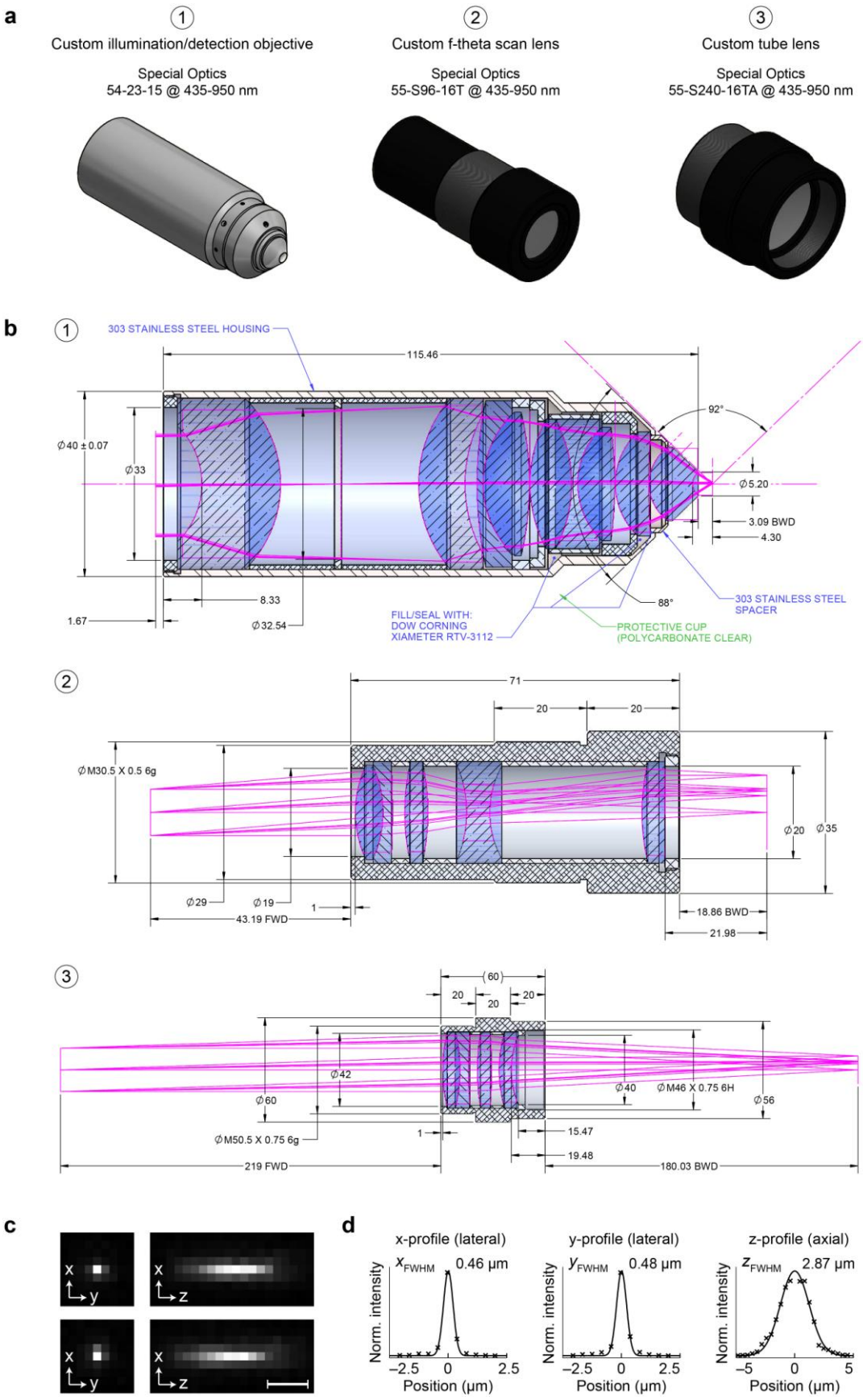
a
1
Custom illumination/detection objective
Special Optics
54-23-15 @ 435-950 nm
2
Custom f-theta scan lens
Special Optics
55-S96-16T @ 435-950 nm
3
Custom tube lens
Special Optics
55-S240-16TA @ 435-950 nm
b
1
303 STAINLESS STEEL HOUSING
115.46
92°
Ø40 ±0.07
Ø33
Ø5.20
3.09 BWD
4.30
8.33
1.67
Ø32.54
88°
303 STAINLESS STEEL SPACER
FILL/SEAL WITH: DOW CORNING XIAMETER RTV-3112
PROTECTIVE CUP (POLYCARBONATE CLEAR)
2
71
20
20
ØM30.5 X 0.5 6g
Ø20
Ø35
Ø29
Ø19
1
43.19 FWD
18.86 BWD
21.98
3
60
20
20
20
Ø42
Ø60
Ø40
ØM46 X 0.75 6H
Ø56
ØM50.5 X 0.75 6g
1
15.47
19.48
219 FWD
180.03 BWD
c
x
y
x
z
x
y
x
z
d
x-profile (lateral)
$x_{FWHM}$ 0.46 µm
Norm. intensity
−2.5
0
2.5
Position (µm)
y-profile (lateral)
$y_{FWHM}$ 0.48 µm
Norm. intensity
−2.5
0
2.5
Position (µm)
z-profile (axial)
$z_{FWHM}$ 2.87 µm
Norm. intensity
−5
0
5
Position (µm)

**Supplementary Figure 3**

Technical drawings of IsoView custom optical components.

(**a**) The IsoView microscope uses three types of custom optical components: objectives for both light-sheet illumination and fluorescence detection, f-theta scan lenses and detection tube lenses. These components have been jointly designed and modeled for optimal combined performance in the illumination and detection arms of the IsoView microscope, minimizing spherical and chromatic aberrations and maximizing telecentricity. The most critical custom components are the objectives, which offer (1) diffraction-limited performance over a wide wavelength range (435-950 nm) for multi-color imaging, (2) small telecentric error (< 0.1º) for efficient confocal line scanning, (3) large field-of-view (800 µm) and long working distance (3.09 mm) for imaging large specimens using various specimen preparation techniques, (4) a light-weight design (361 g) for fast volumetric imaging with objective piezo positioners, (5) a cone angle smaller than 90º, which allows simultaneous use of four objectives aimed at a common focal point in a perpendicular arrangement, and (6) a numerical aperture (0.714) close to the theoretical maximum given the geometrical constrains (**Supplementary Fig. 5**). Higher numerical apertures can be achieved by sacrificing field-of-view or volumetric scan range, but apertures are generally constrained in four-view imaging by the requirement of an objective cone angle below 90º. (**b**) Technical drawings of the custom optical components shown in **a**. (**c**) System PSFs measured with IsoView custom objectives using fluorescent beads located at the surface of an agarose cylinder. Two representative examples are shown. (**d**) Gaussian fits and respective three-dimensional FWHM measurements of the IsoView system PSF. When imaging eGFP fluorescence using a 525/50-nm band-pass filter, the average emission wavelength is $\lambda = 0.519$ µm. Thus, measured lateral resolution is in good agreement with the theoretical Abbe limit of 0.44 µm ($0.61 \times \lambda / 0.714$).

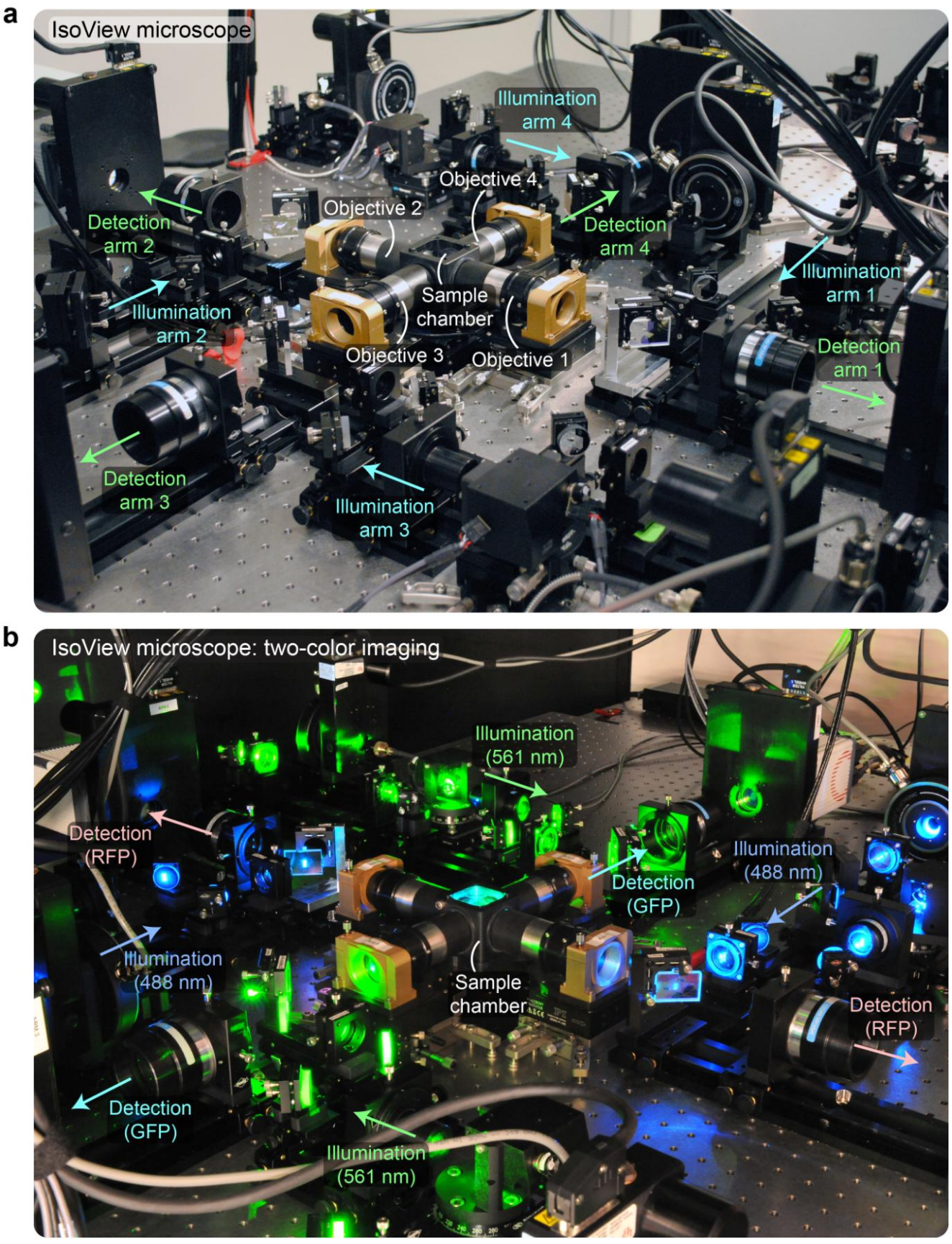
a
IsoView microscope
Illumination arm 4
Objective 4
Objective 2
Detection arm 2
Detection arm 4
Illumination arm 1
Sample chamber
Illumination arm 2
Objective 3
Objective 1
Detection arm 1
Detection arm 3
Illumination arm 3
b
IsoView microscope: two-color imaging
Illumination (561 nm)
Detection (RFP)
Detection (GFP)
Illumination (488 nm)
Illumination (488 nm)
Sample chamber
Detection (RFP)
Detection (GFP)
Illumination (561 nm)

**Supplementary Figure 4**

Implementation of the IsoView light-sheet microscope.

(**a**) Photograph of the core of the IsoView light-sheet microscope. (**b**) Photograph of the core of the IsoView light-sheet microscope during four-view, two-color imaging (IsoView mode 3, see **Fig. 1d**) with 488 nm and 561 nm excitation wavelengths. The snapshot shows the microscope during the first phase of the imaging cycle; in the second phase, wavelength assignments in illumination and detection arms are switched in order to acquire the complementary set of colors and views. Together, phases one and two yield four-view data sets for both spectral bands.

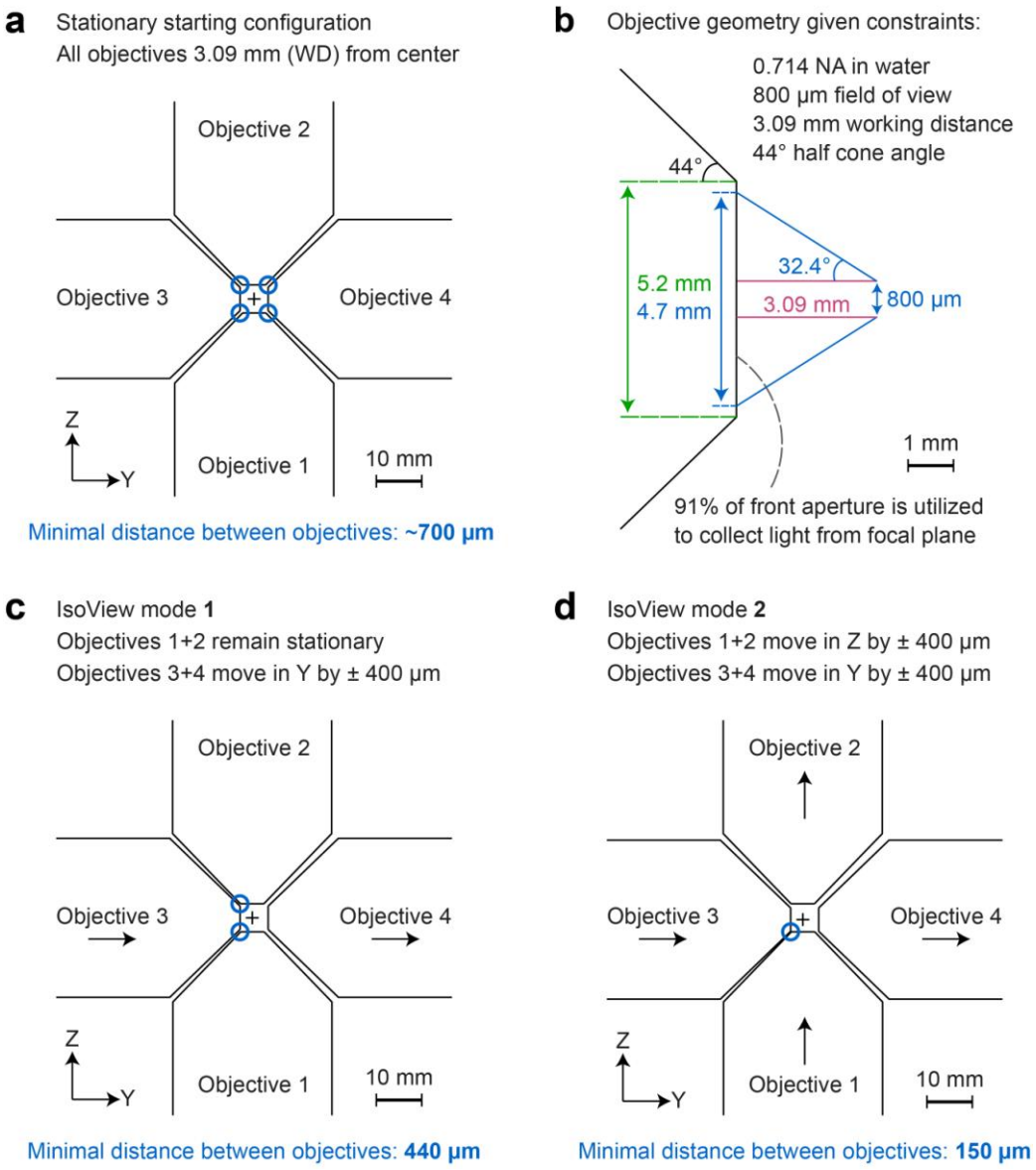


**Supplementary Figure 5**

Geometrical considerations in IsoView objective design.

(**a**) Schematic top view of the four-objective arrangement in the IsoView microscope. When positioning all objectives symmetrically around the center of the sample chamber, the minimal distance between neighboring objectives is approximately 700 µm. WD = working distance. (**b**) Schematic side view of an IsoView objective. Black lines indicate the geometrical outline of the objective nose piece. Magenta, green and blue lines mark geometrical distances and angles. Numerical aperture (0.714) is close to the theoretical maximum, considering the geometrical constraints imposed by a field-of-view of 800 µm, a working distance of 3.09 mm (shown in magenta) and a piezo scan range of 800 µm. As illustrated in panels **c** and **d**, the minimal distance between neighboring objectives is 440 µm or 150 µm when imaging a volume of 800 × 800 × 800 $\mu m^3$ in IsoView modes 1 or 2, respectively. (**c**) Schematic top view of the four-objective arrangement in the IsoView microscope during an imaging experiment performed in IsoView mode 1 (sequential four-view imaging). The snapshot represents the microscope state at the end of a volumetric imaging sequence. When imaging a volume of 800 × 800 × 800 $\mu m^3$ in this mode, the minimal distance between neighboring objectives is 440 µm. Black arrows next to objective labels indicate objective movement directions during the volume scan. (**d**) As in **c** but for IsoView mode 2 (simultaneous four-view imaging). In this scenario, the minimal distance between neighboring objectives is 150 µm when imaging a volume of 800 × 800 × 800 $\mu m^3$. Black arrows next to objective labels indicate objective movement directions during the volume scan.

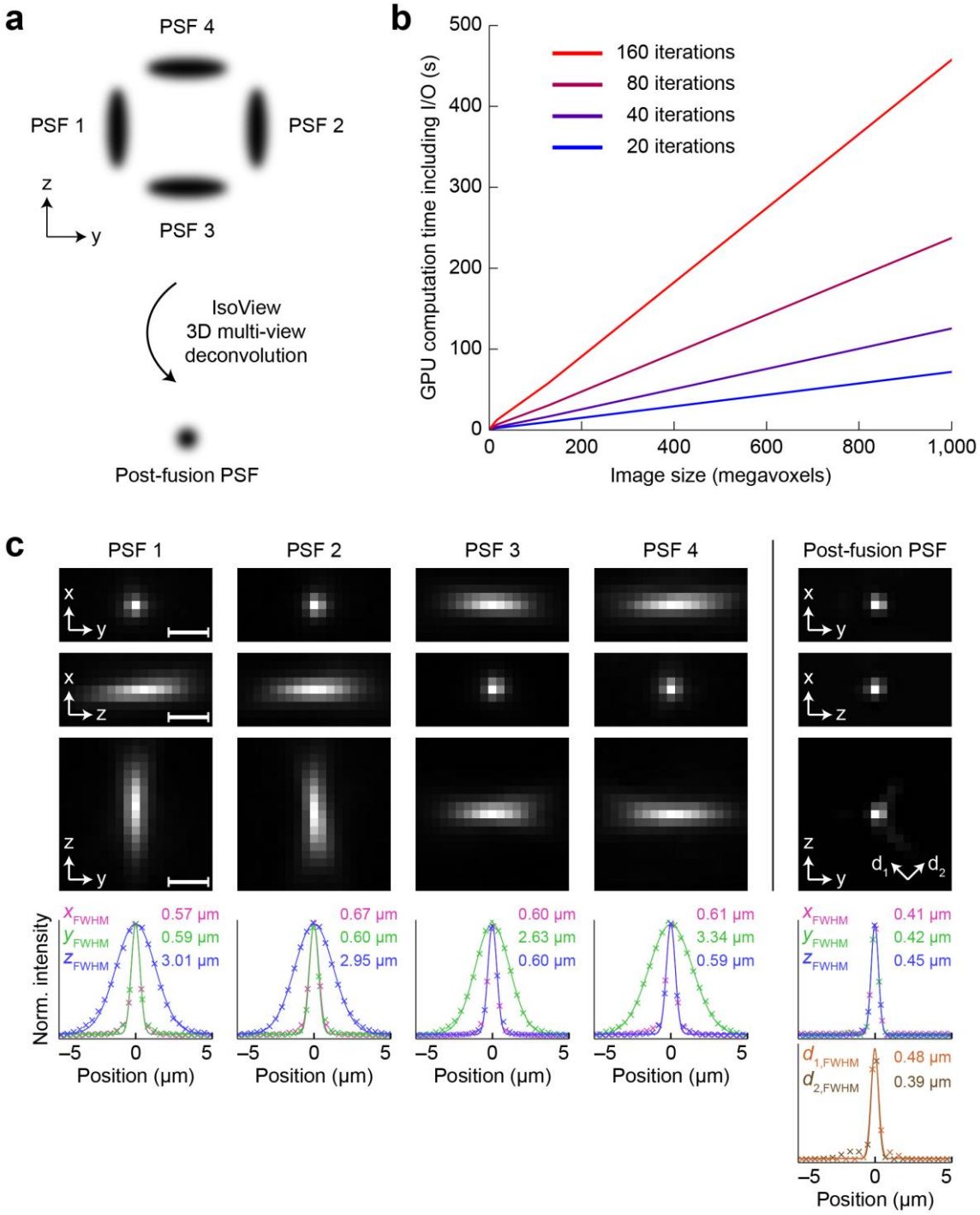


**Supplementary Figure 6**

IsoView point-spread functions and multiview deconvolution.

(**a**) Lateral and axial dimensions of anisotropic PSFs in views 1 and 2 are flipped with respect to those of views 3 and 4. Improved resolution and isotropy are achieved by combining all views using three-dimensional multi-view image deconvolution. (**b**) Processing time required to perform four-view image deconvolution with the IsoView image deconvolution software, shown as a function of three-dimensional image size and for four different numbers of iterations of the Lucy-Richardson algorithm (20, 40, 80 and 160). Processing was performed on a single computer workstation equipped with four Nvidia K20x Tesla GPUs. Image size is represented by the voxel

count in each single-view image stack. The corresponding computation time measurements also inform about processing time requirements for time-lapse data sets with an arbitrary number of time points. For example, processing a four-view data set with $1024^3$ voxels per view and 16-bit image depth (i.e. 8 GB of image data per time point) takes 128 seconds for 40 Lucy-Richardson iterations, the typical setting used in our study. Thus, processing a typical 10 TB time-lapse data set (1,250 time points, with 8 GB of image data per time point) takes 45.7 hours of GPU time, including I/O operations. (**c**) Top: Experimental PSFs for views 1-4 ("PSF 1-4") and final PSF after multi-view deconvolution ("Post-fusion PSF"). Fluorescently labeled beads were imaged at the center of a 1.5-mm-thick agarose cylinder. Bottom: Gaussian fits and FWHM measurements for the PSFs shown above. Post-fusion PSF analysis considers diagonal dimensions of the y-z image plane (see also Swoger *et al*. 2007, *Optics Express*). Scale bars, 2 µm (**c**).

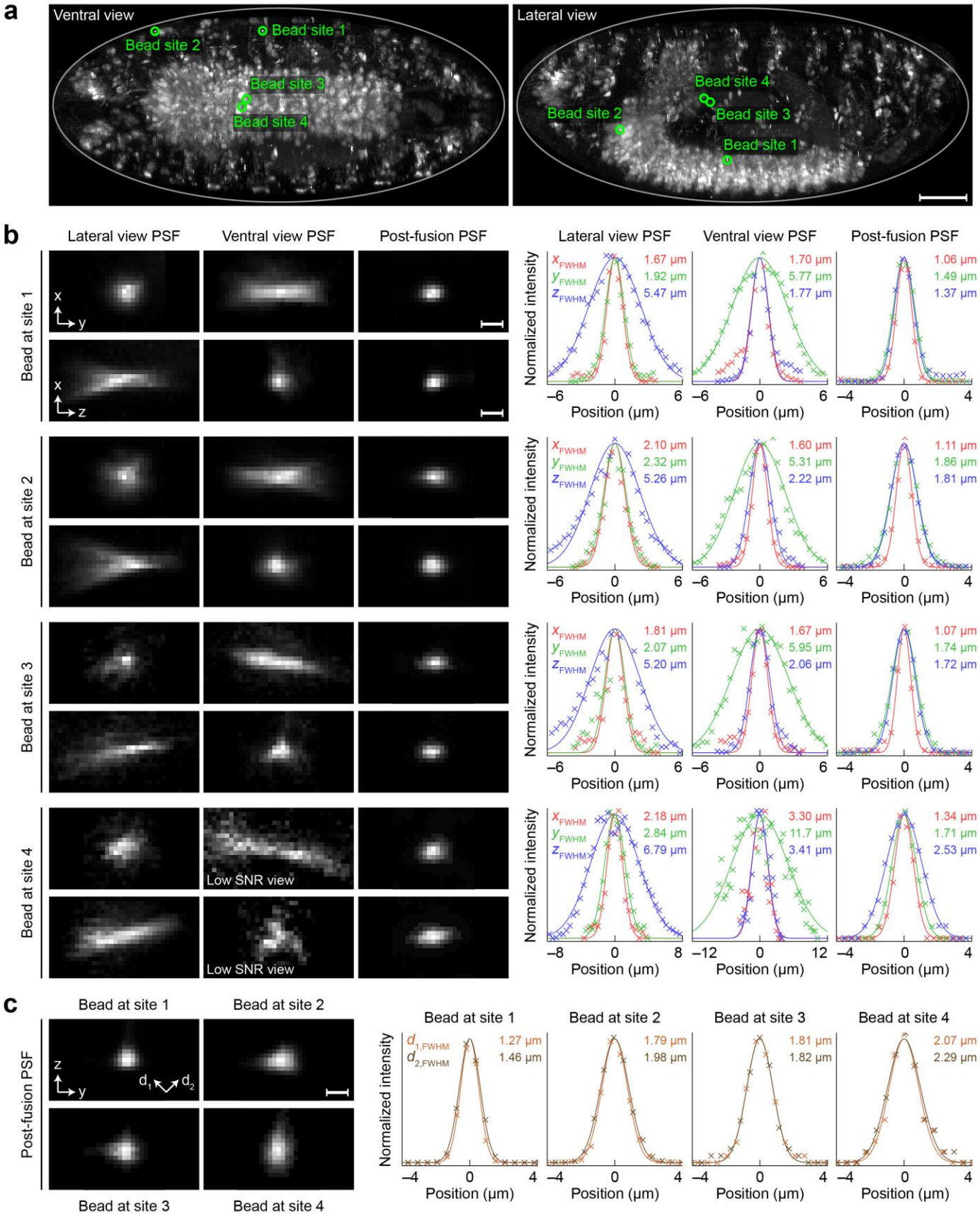


Nature Methods: doi:10.1038/nmeth.3632

**Supplementary Figure 7**

IsoView PSFs in a live *Drosophila* embryo.

(**a**) Ventral- and lateral-view maximum-intensity projections of a stage 17 *Drosophila* embryo expressing the calcium indicator GCaMP6s throughout the nervous system. The embryo was injected with fluorescent beads to assess IsoView point spread functions (PSFs) *in vivo* at different depths in the embryo. Four bead sites are marked by green circles, including two sites in more superficial regions (1 and 2) and two sites at the center of the embryo (3 and 4), i.e. in the deepest and optically most challenging region of the embryo. (**b**) Left: Experimentally measured PSFs in raw views (labeled “Lateral view PSF” and “Ventral view PSF”, representing the microscope’s orthogonal optical axes) and the final PSF resulting after multi-view deconvolution (“Post-fusion PSF”). The fluorescent bead at site 4 represents a worst-case scenario with respect to the associated imaging challenges: not only is the bead located in the deepest part of the embryo, but it is also found at a location between brain lobes and ventral nerve cord that it difficult to access by the IsoView detection arms aligned with the dorso-ventral axis. Consequently, this view provides the lowest signal-to-noise ratio across all examples. Right: Gaussian fits and respective FWHM measures of PSFs for all views and spatial dimensions. Chi-squared ($\chi^2$) residuals for all fits are between 0.0062 and 0.69. Statistics are based on distributions with 16 degrees of freedom (for x-y dimensions in lateral view PSFs, x-z dimensions in ventral view PSFs, all dimensions in post-fusion PSFs) or 42 degrees of freedom (for z dimension in lateral view PSFs, y dimension in ventral view PSFs). Thus, using Pearson's chi-squared test, the probability *p* of the Gaussian fits to represent poor fits is below $10^{-10}$ in all cases. When comparing signal strengths at locations near the surface of the embryo (< 20 µm depth) to those at locations near the center of the embryo (100 µm depth), bead fluorescence intensities decrease on average by a factor of 5 in the raw views and by a factor of 6 in the multi-view deconvolved IsoView data. (**c**) y-z images and Gaussian fits along diagonal dimensions for the post-fusion PSFs shown in (b). Scale bars, 2 µm (b,c), 50 µm (a).

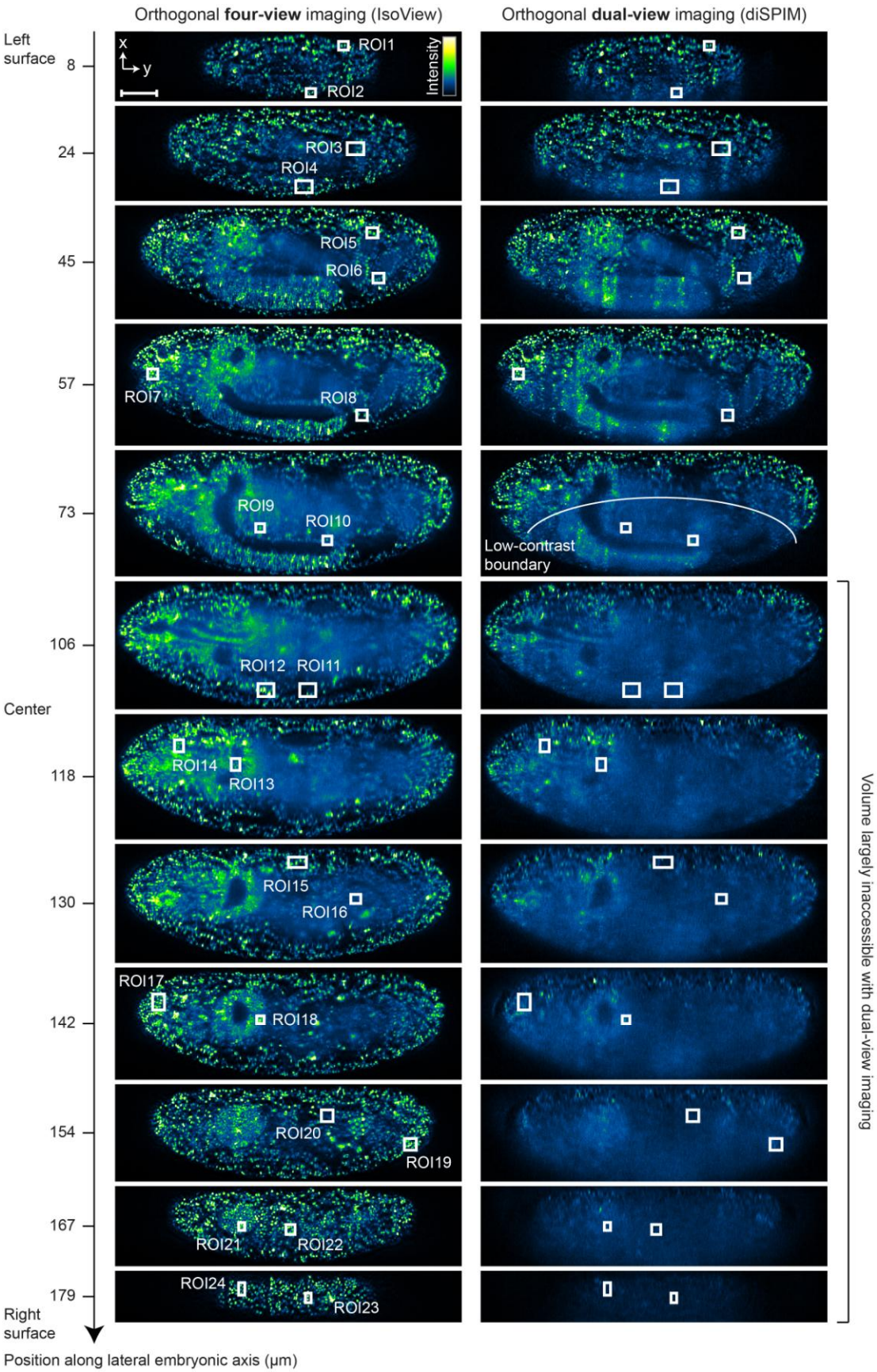


Nature Methods: doi:10.1038/nmeth.3632

**Supplementary Figure 8**

Comparison of four-view and orthogonal dual-view imaging (overview).

Side-by-side comparison of multi-view deconvolved image data obtained with orthogonal four-view imaging (IsoView) and orthogonal dual-view imaging (following the diSPIM concept developed by Wu *et al*. 2013, *Nature Biotechnology*), for a live stage 17 *Drosophila* embryo expressing mRFP1 in all cell nuclei. The images show a depth series along the lateral axis of the 200-µm-thick embryo. All images were acquired with the IsoView microscope, using either two (diSPIM) or all four (IsoView) of the microscope's imaging arms. Objectives were facing the dorsal, ventral, lateral-left or lateral-right sides of the embryo, using dorsal and lateral-left views for diSPIM-like dual-view deconvolution. Imaging settings were otherwise identical, including laser power settings, exposure time and spatial sampling. Image deconvolution was performed with identical point spread functions and number of iterations of the Lucy-Richardson algorithm. **Supplementary Figs. 9** and **10** provide enlarged views of x-y and x-z image sections for 24 different regions throughout the embryo (marked by white boxes labeled "ROI1" to "ROI24"). Due to light scattering and light absorption by the embryo, orthogonal dual-view imaging captures approximately one quarter of the sample volume at high spatial resolution, whereas orthogonal four-view imaging provides close to complete coverage of the embryo. We note that IsoView achieves this improvement in high-resolution coverage without decreasing temporal resolution, which is essential for system-level functional imaging with calcium indicators (**Supplementary Videos 2-4**) or developmental imaging of fast cellular dynamics in the *Drosophila* embryo (**Supplementary Videos 6** and **7**). Scale bar, 50 µm.

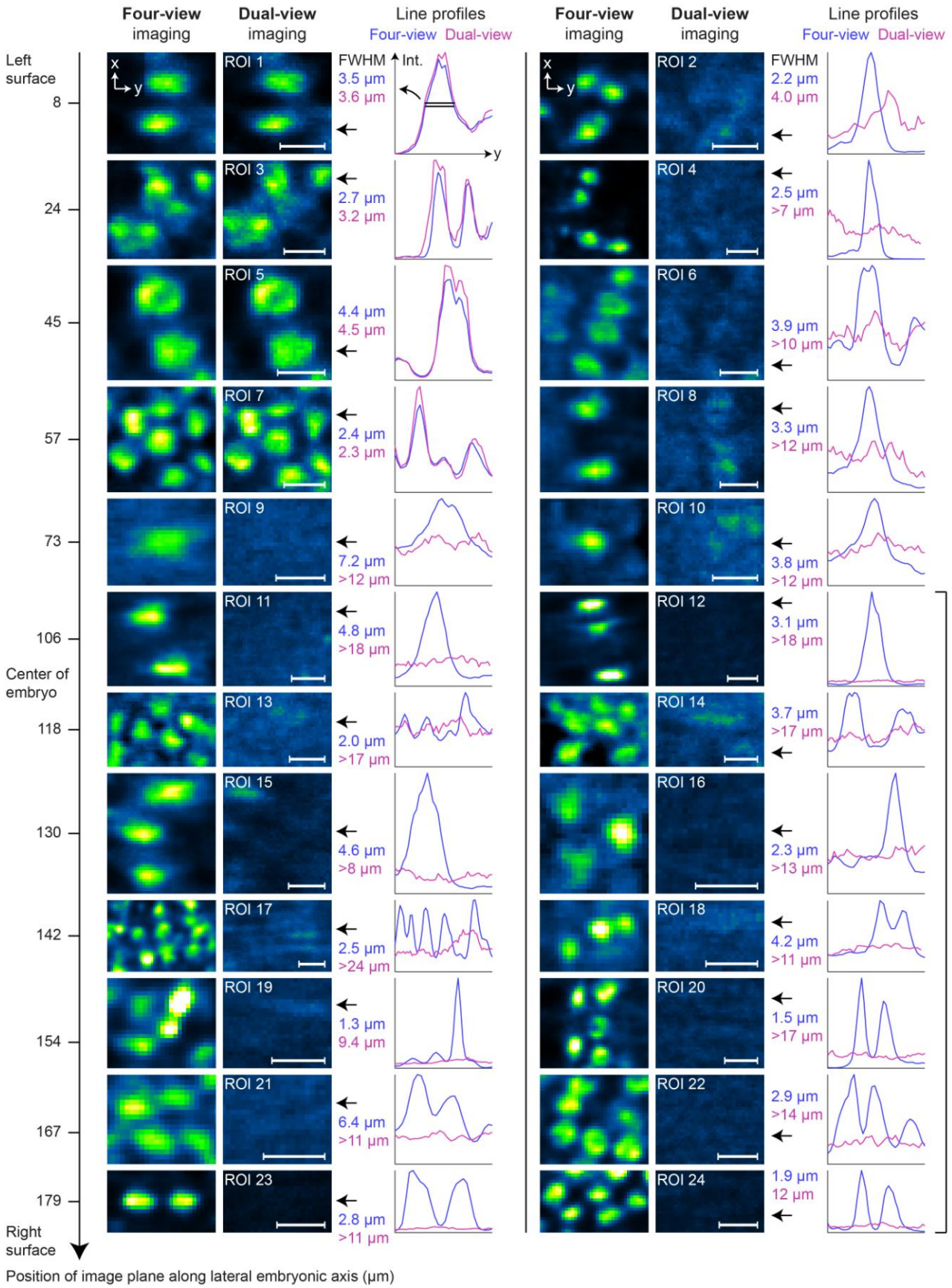
Four-view imaging
Dual-view imaging
Line profiles
Four-view Dual-view
Four-view imaging
Dual-view imaging
Line profiles
Four-view Dual-view
Left surface
Center of embryo
Right surface
8
24
45
57
73
106
118
130
142
154
167
179
x
y
FWHM
Int.
ROI 1
3.5 µm
3.6 µm
ROI 2
2.2 µm
4.0 µm
ROI 3
2.7 µm
3.2 µm
ROI 4
2.5 µm
>7 µm
ROI 5
4.4 µm
4.5 µm
ROI 6
3.9 µm
>10 µm
ROI 7
2.4 µm
2.3 µm
ROI 8
3.3 µm
>12 µm
ROI 9
7.2 µm
>12 µm
ROI 10
3.8 µm
>12 µm
ROI 11
4.8 µm
>18 µm
ROI 12
3.1 µm
>18 µm
ROI 13
2.0 µm
>17 µm
ROI 14
3.7 µm
>17 µm
ROI 15
4.6 µm
>8 µm
ROI 16
2.3 µm
>13 µm
ROI 17
2.5 µm
>24 µm
ROI 18
4.2 µm
>11 µm
ROI 19
1.3 µm
9.4 µm
ROI 20
1.5 µm
>17 µm
ROI 21
6.4 µm
>11 µm
ROI 22
2.9 µm
>14 µm
ROI 23
2.8 µm
>11 µm
ROI 24
1.9 µm
12 µm
Volume largely inaccessible with dual-view imaging
Position of image plane along lateral embryonic axis (µm)

**Supplementary Figure 9**

Comparison of four-view and orthogonal dual-view imaging (*x*-*y* sections).

Enlarged views of x-y image sections for the 24 regions marked by white boxes in **Supplementary Fig. 8**. The images show a side-by-side comparison of multi-view deconvolved image data obtained with orthogonal four-view imaging (IsoView approach) and orthogonal dual-view imaging (diSPIM approach) for a live stage 17 *Drosophila* embryo expressing mRFP1 in all cell nuclei. All image data were acquired with the IsoView microscope, using either two (diSPIM) or all four (IsoView) of the microscope's imaging arms. Imaging and multi-view deconvolution settings were otherwise identical. The line profiles next to the image panels represent normalized intensity profiles along the image y-axis at the respective x-locations indicated by the black arrows. Line profiles are shown both for dual-view imaging (magenta) and four-view imaging (blue). Numbers provided next to the line profiles indicate full-width-at-half-maximum (FWHM) measurements for the left-most intensity peak at the respective x-location. The optical axes of the two objectives employed in dual-view imaging were aligned with the dorsoventral and lateral embryonic axes. The 24 regions analyzed in this comparison cover a wide range of illumination and detection path lengths across the embryo, including regions with diSPIM illumination and detection paths up to 60 µm (ROIs 1, 3, 5 and 7), regions with dorsoventral paths >60 µm and lateral paths <60 µm (ROIs 2, 4, 6 and 8), regions with dorsoventral paths <60 µm and lateral paths >60 µm (ROIs 13-15, 17, 18, 20 and 21-24) and regions with dorsoventral and lateral paths >60 µm (ROIs 9, 10-12, 16 and 19). Dual-view imaging provides excellent spatial resolution up to a maximum depth of approximately 60 µm, yielding high-resolution coverage of approximately one quarter of the specimen. Four-view imaging typically achieved identical spatial resolution in these regions, although a quarter of our data points attest to higher resolution in the IsoView data. These differences are likely rooted in the fact that the respective regions are captured in sufficiently high quality by three out of the four views provided by IsoView, thus adding a third source of high-frequency image content. For illumination and detection path lengths exceeding 60 µm, resolution and signal strength in dual-view imaging degrade substnatially and cellular resolution is typically compromised. In contrast, high-resolution coverage of almost the entire embryo is achieved with four-view imaging, consistent with the intuition that opposing views in IsoView should effectively double optical access along both illumination and detection axes. Notably, four-view imaging still resolves neighboring cell nuclei as distinct objects in some the deepest regions of the embryo with optical path lengths close to 100 µm (ROIs 13 and 16). Scale bars, 5 µm.

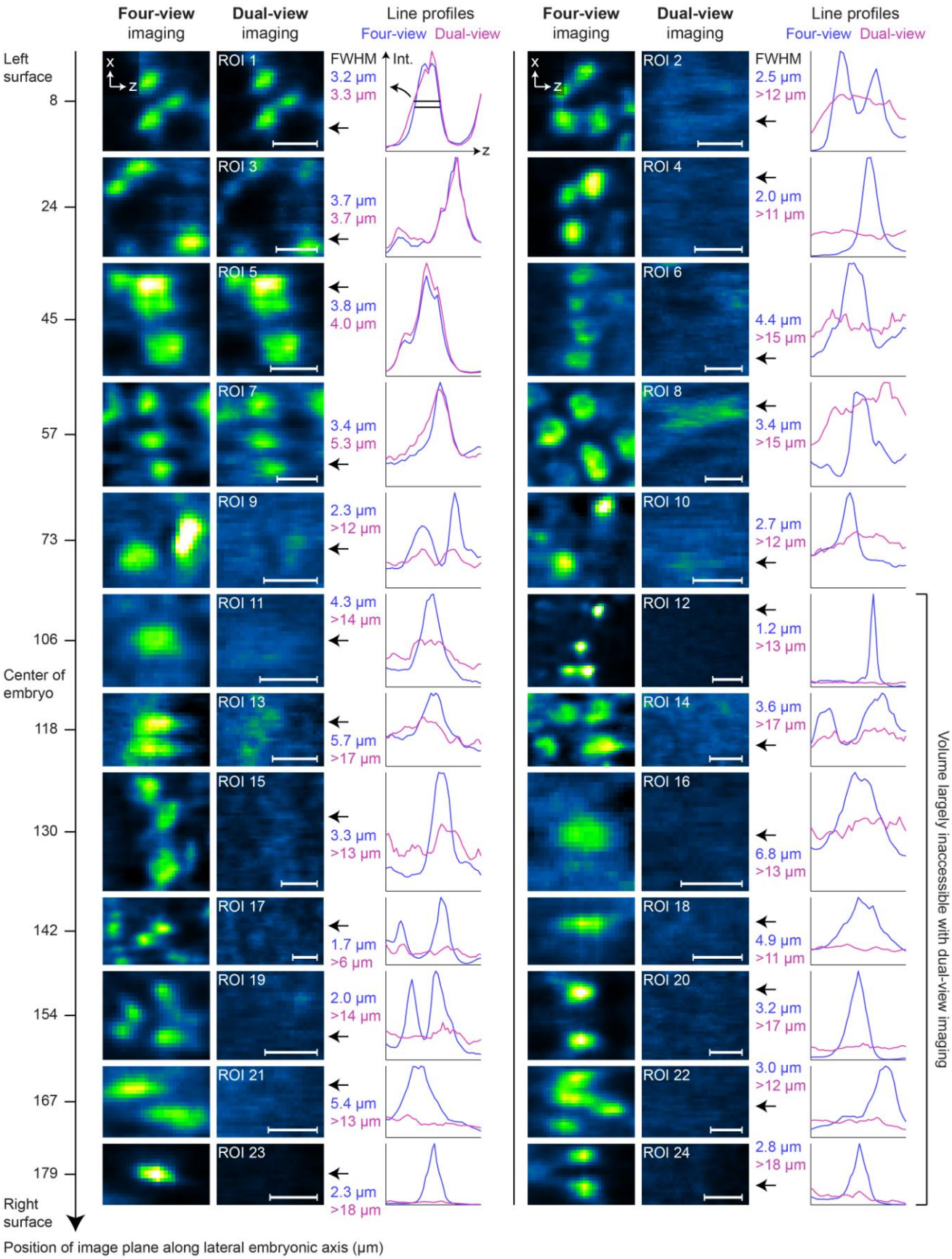


Nature Methods: doi:10.1038/nmeth.3632

**Supplementary Figure 10**

Comparison of four-view and orthogonal dual-view imaging (*x*-*z* sections).

Visualization as in **Supplementary Fig. 9**, but for enlarged views of x-z image sections for the 24 regions marked by white boxes in **Supplementary Fig. 8**. We note that all image panels represent individual image slices, rather than volume projections, and thus x-z and x-y sections shown here and in **Supplementary Fig. 9** only share a subset of cell identities. Scale bars, 5 µm.

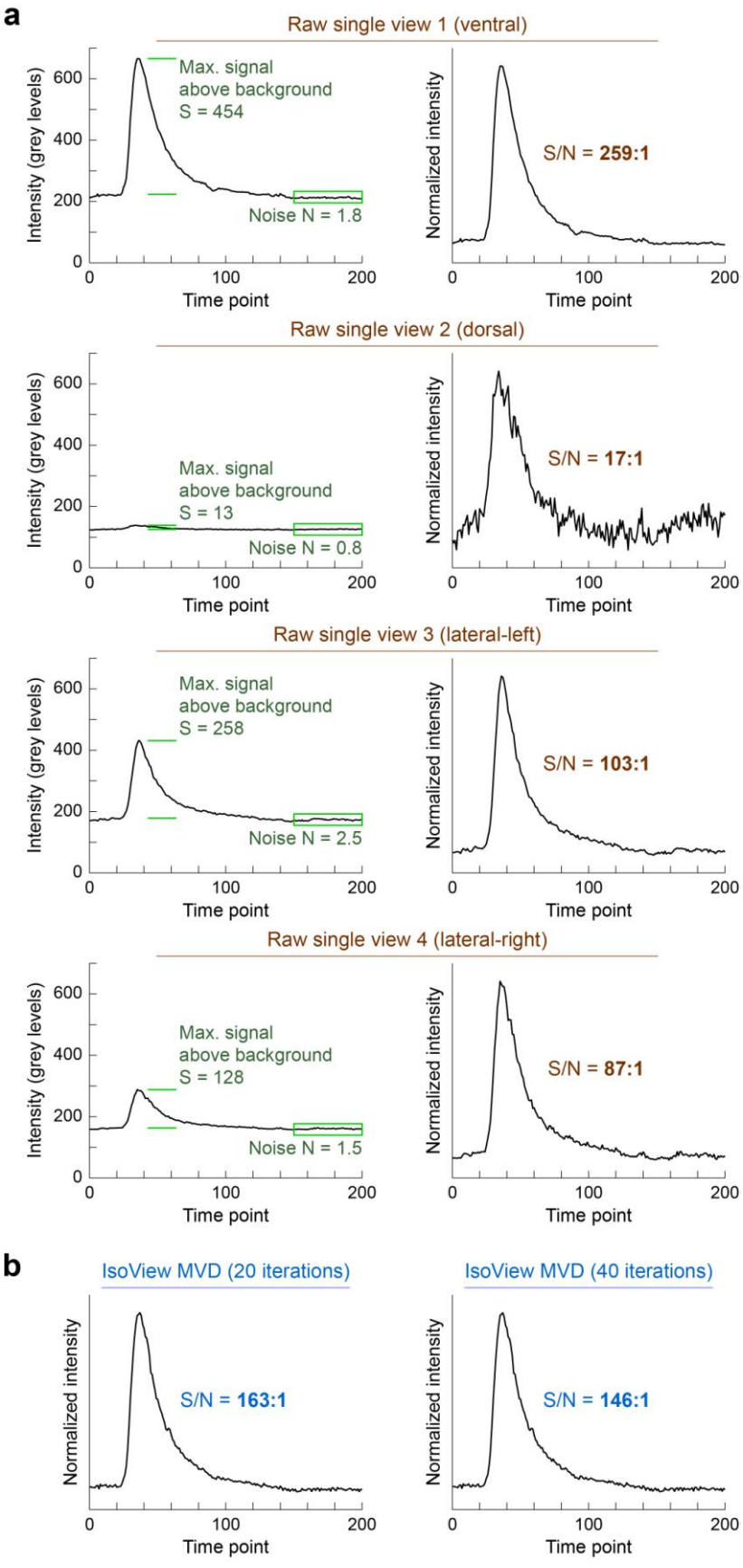
a
Raw single view 1 (ventral)
Max. signal above background S = 454
Noise N = 1.8
S/N = 259:1
Raw single view 2 (dorsal)
Max. signal above background S = 13
Noise N = 0.8
S/N = 17:1
Raw single view 3 (lateral-left)
Max. signal above background S = 258
Noise N = 2.5
S/N = 103:1
Raw single view 4 (lateral-right)
Max. signal above background S = 128
Noise N = 1.5
S/N = 87:1
Intensity (grey levels)
Normalized intensity
Time point
b
IsoView MVD (20 iterations)
S/N = 163:1
IsoView MVD (40 iterations)
S/N = 146:1

**Supplementary Figure 11**

Fidelity and noise statistics in GCaMP fluorescence traces.

Side-by-side comparison of single-neuron fluorescence traces and noise statistics for single-view image data (a) and multi-view deconvolved IsoView image data (b). All plots show traces for the same time window and for the same soma located in the posterior ventral nerve cord of a stage 17 *Drosophila* embryo. Across the four single views (a), signal-to-noise ratio is highest in the ventral-view image data, followed by image data from the two lateral views. We note that the VNC neuron cannot be resolved by imaging from the dorsal side. Extracting a fluorescence trace from the dorsal-view image data for the volume corresponding to the soma volume identified in the ventral-view image data yields a very weak signal (30-fold reduced amplitude) with 15-fold reduced signal-to-noise ratio (second row in (a)). Signal fidelity and noise statistics in the multi-view deconvolved IsoView data are comparable to average performance of the respective two best single views. Increasing the number of iterations of the Lucy-Richardson deconvolution algorithm leads to a slight reduction in signal-to-noise ratio (see left vs. right plots in (b)).

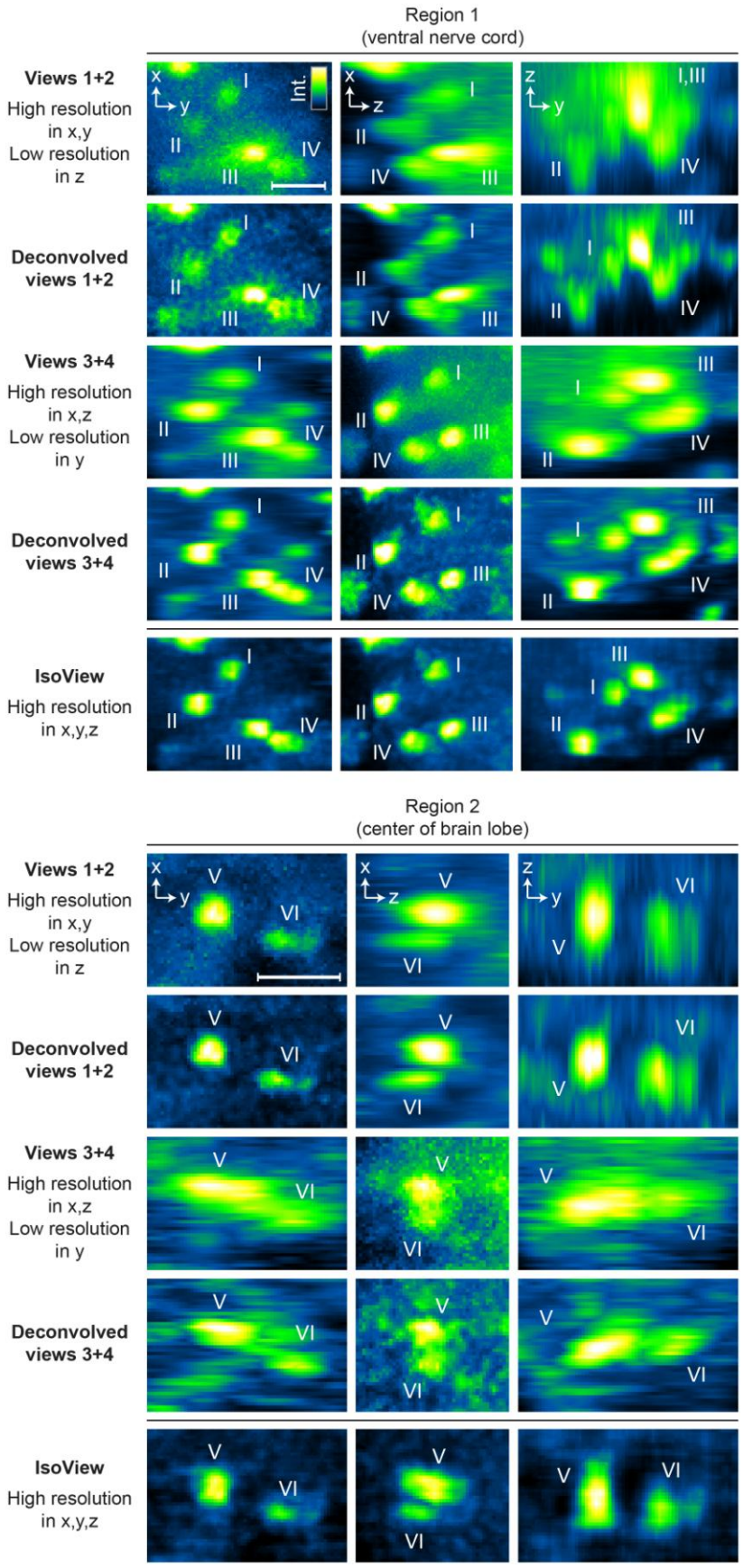


Nature Methods: doi:10.1038/nmeth.3632

**Supplementary Figure 12**

Comparison of single-view and IsoView deconvolution (functional imaging).

Side-by-side comparison of raw anisotropic image data, single-view deconvolved image data and multi-view deconvolved IsoView image data for optical sections of the specimen shown in **Figs. 2** and **3**, using the same false-color look-up-table. Single-view and multi-view deconvolution were performed with identical point spread functions and number of iterations of the Lucy-Richardson algorithm. The comparison includes examples from two different deep regions of the nervous system (dorsal region of the ventral nerve cord and center of a brain lobe). Roman numerals identify locations of somas with high GCaMP6s fluorescence. Single-view deconvolution (rows labeled “Deconvolved views 1+2”, “Deconvolved views 3+4”) improved resolution compared to raw image data (rows labeled “Views 1+2”, “Views 3+4”) but is outperformed by multi-view deconvolution (rows labeled “IsoView”). We further note that single-view deconvolution has a stronger tendency of introducing image artifacts related to noise in the raw image data (for the same number of iterations of the Lucy-Richardson algorithm), in particular for those views with respectively lower signal-to-noise ratio. To take full advantage of IsoView image data, we thus recommend combining the four individual views by multi-view deconvolution. Scale bars, 10 μm.

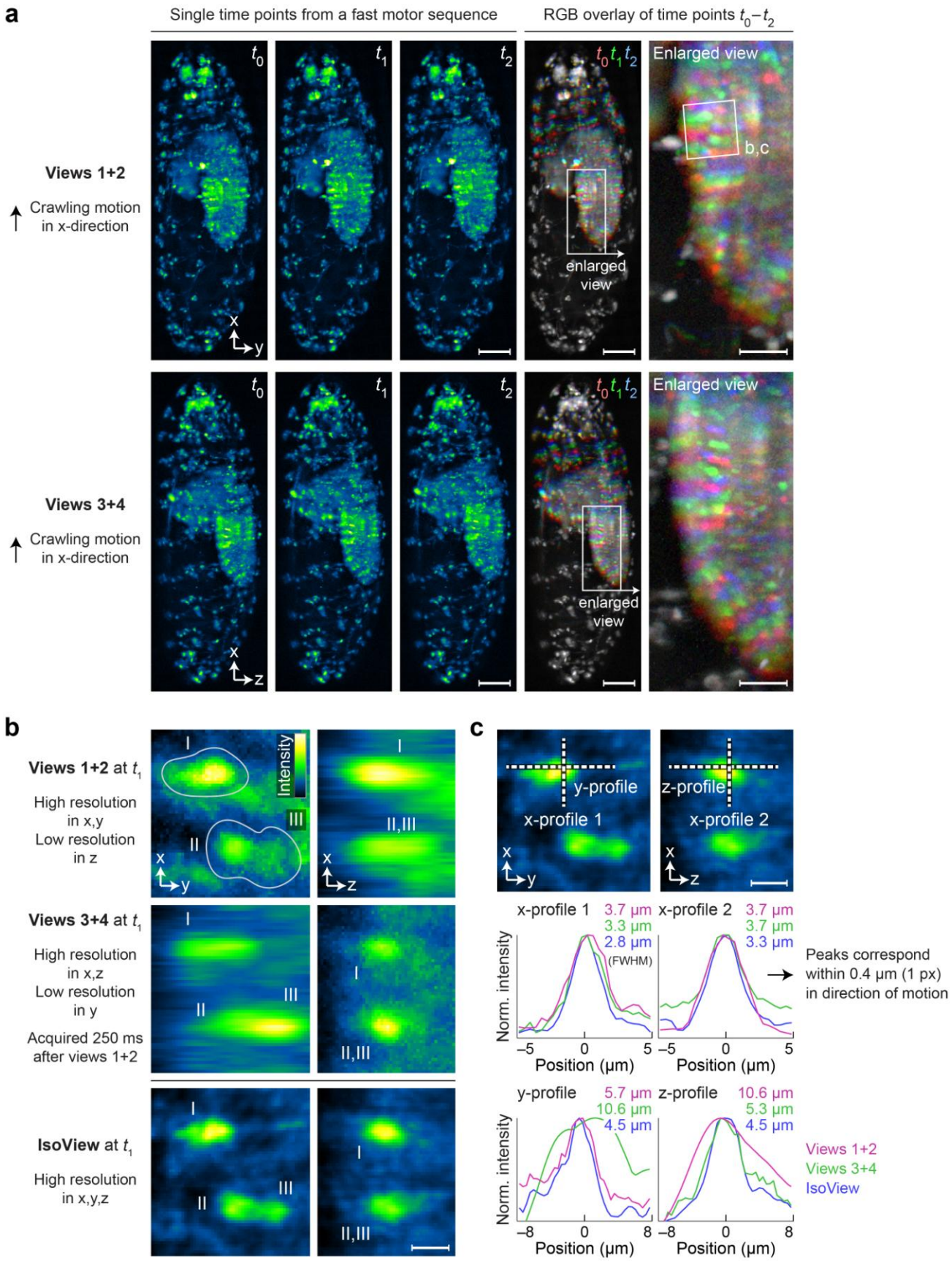


Nature Methods: doi:10.1038/nmeth.3632

**Supplementary Figure 13**

Accurate registration and deconvolution during sample movements.

(**a**) Columns 1-3: Maximum-intensity projections of raw IsoView image data of an early first instar *Drosophila* larva expressing the calcium indicator GCaMP6s throughout the nervous system. Projections are shown along view axes 1+2 and 3+4, prior to multi-view deconvolution, for consecutive time points in a fast motor sequence. A wave of muscle contractions is traveling through the larva and reaches peak speed at time point $t_1$. Columns 4-5: RGB color overlays of time points $t_0$, $t_1$ and $t_2$ shown in columns 1-3, visualizing the magnitude of tissue movements during this time interval. The panels in column 5 show enlarged views of the anatomical region most strongly affected by these movements (a section of the ventral nerve cord). (**b**) Side-by-side comparison of raw, anisotropic image data and multi-view deconvolved IsoView image data for an optical section in the region highlighted in (a). All views were processed at the whole-embryo level with the content-based multi-view registration and deconvolution method described in the Online Methods. (**c**) Side-by-side comparison of intensity profiles along x-, y- and z-axes extracted from raw, anisotropic image data and multi-view deconvolved IsoView image data, respectively. The locations of the line plots within each optical section are indicated in the panels shown in the top row. Numerical results listed next to the raw intensity profiles represent FWHM size measures. Line profiles and FWHM measures demonstrate that IsoView image registration and multi-view deconvolution operate accurately even in the presence of substantial sample motion; in particular, intensity peaks along the x-axis (i.e. in the direction of maximum sample motion) correspond within one pixel (0.4 µm) in individual views and multi-view deconvolved IsoView image data. Scale bars, 5 µm (b,c), 20 µm (a, enlarged views), 50 µm (a, whole-embryo views).

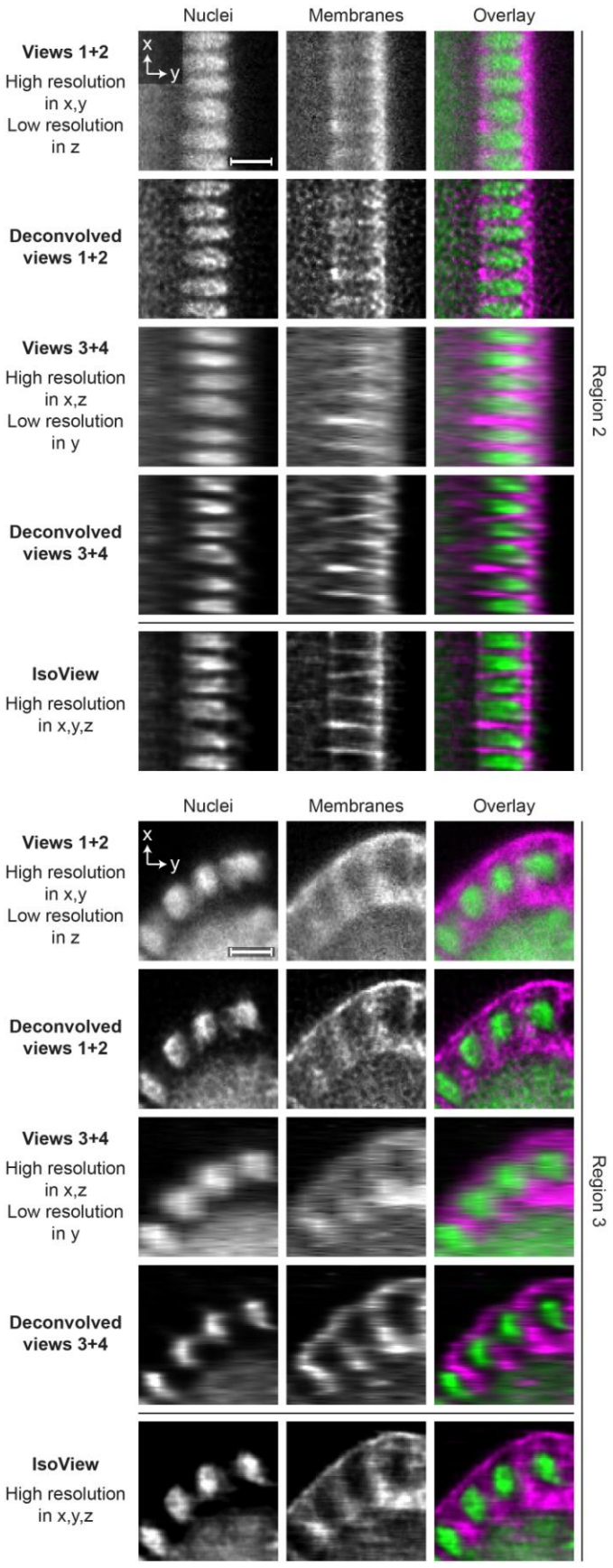
Nuclei
Membranes
Overlay
Views 1+2
High resolution in x,y
Low resolution in z
x
y
Deconvolved views 1+2
Views 3+4
High resolution in x,z
Low resolution in y
Deconvolved views 3+4
IsoView
High resolution in x,y,z
Region 2
Nuclei
Membranes
Overlay
Views 1+2
High resolution in x,y
Low resolution in z
x
y
Deconvolved views 1+2
Views 3+4
High resolution in x,z
Low resolution in y
Deconvolved views 3+4
IsoView
High resolution in x,y,z
Region 3

**Supplementary Figure 14**

Comparison of single-view and IsoView deconvolution (developmental imaging 1).

Side-by-side comparison of raw anisotropic image data, single-view deconvolved image data and multi-view deconvolved IsoView image data for optical sections of the specimen shown in **Fig. 5**. Single-view and multi-view deconvolution were performed with identical point spread functions and number of iterations of the Lucy-Richardson algorithm. Single-view deconvolution (rows labeled “Deconvolved views 1+2”, “Deconvolved views 3+4”) improves resolution compared to raw image data (rows labeled “Views 1+2”, “Views 3+4”) but is outperformed by multi-view deconvolution (rows labeled “IsoView”). Importantly, single-view deconvolution also fails to recover morphological features that require multiple views to be properly resolved, such as the cell membranes shown in region 2: views 3+4 contribute membrane features laterally demarcating neighboring cells, whereas views 1+2 contribute membrane features at apical and basal ends of cells. We further note that single-view deconvolution has a stronger tendency of introducing image artifacts related to noise in the raw image data (for the same number of iterations of the Lucy-Richardson algorithm), in particular for those views with respectively lower signal-to-noise ratio. To take full advantage of IsoView image data, we thus recommend combining the four individual views by multi-view deconvolution. Scale bars, 10 µm.

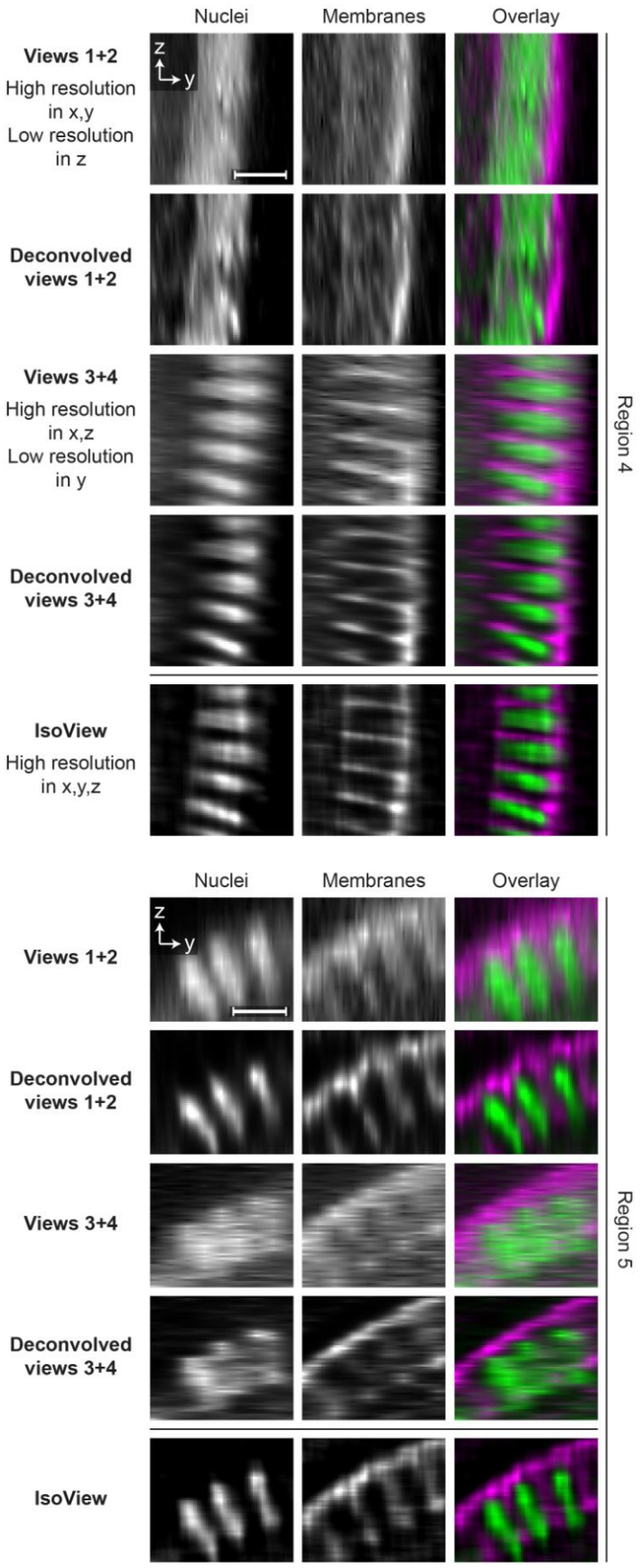
Nuclei
Membranes
Overlay
Views 1+2
High resolution in x,y
Low resolution in z
Deconvolved views 1+2
Views 3+4
High resolution in x,z
Low resolution in y
Deconvolved views 3+4
IsoView
High resolution in x,y,z
Region 4
z
y
Nuclei
Membranes
Overlay
Views 1+2
Deconvolved views 1+2
Views 3+4
Deconvolved views 3+4
IsoView
Region 5
z
y

**Supplementary Figure 15**

Comparison of single-view and IsoView deconvolution (developmental imaging 2).

Comparative visualization as in **Supplementary Fig. 14**, but for y-z image cross-sections taken from image data of a gastrulating *Drosophila* embryo (**Supplementary Video 5**). The lower block of image panels ("Region 5") exemplifies a worst-case scenario for four-view imaging: membranes and cell nuclei are oriented close to a 45-degree angle relative to the microscope's two principal imaging axes (y- and z-axes). Thus, for the particular sample geometry encountered here, the four views of the IsoView microscope provide less high-frequency content than available for any other sample geometry (see also Swoger *et al*. 2007, *Optics Express*). The corresponding y-z image cross-sections illustrate that IsoView is nevertheless capable of substantial improvements in overall resolution and resolution isotropy relative to conventional imaging, resolving sub-cellular features such as plasma membranes also in this challenging scenario. Scale bar, 10 µm.

**Supplementary Table 1 |** Components of the IsoView light-sheet microscope

| Module | Component | Product(s) | Manufacturer |
|---|---|---|---|
| Optical table and breadboard | Optical table | Custom ST-UT2 Super SmartTable Top 04SI80903 (5' × 9.0' × 8.0") | Newport |
| | | S-2000 Series 22" isolators with automatic leveling S-2000A-422 (4×) | |
| | | Optical pedestal extension PS-1E-T (4×) | |
| | Breadboard | Custom PG2 precision grade breadboard 04SI80904 (4.0' × 6.0' × 2.32") | Newport |
| | Rail system | SYS 40 and SYS 65 rail and slide system components | OWIS |
| Lasers (two modules) | SOLE-6 engine with dual-fiber head | Solid-state lasers: 488 nm, 515 nm | Omicron Laserage |
| | | DPSS lasers: 561 nm, 594 nm | |
| Illumination sub-systems (four modules) | High-speed laser shutter | VS14S2ZM1-100 with AlMgF2 coating | Uniblitz |
| | | VMM-D3 three-channel driver | |
| | Illumination filter wheel | 96A351 filter wheel | Ludl |
| | | MAC6000 DC servo controller | |
| | | NDQ neutral density filters: OD 1.5, OD 3.0 | Melles Griot |
| | | Laser cleanup notch filters: 488/10, 514/10, 561/10, 594/10 | Chroma |
| | Relay lens pair | 49-363-INK, 49-356-INK | Edmund Optics |
| | Dual-axis laser scanner | 6215HSM40B galvanometer scanner | Cambridge Technology |
| | | MicroMax 673XX dual-axis integrating servo driver amplifier | |
| | | 6 mm XY mirror set, mount and interconnect cables | |
| | | MK320S-24 power supply | Astrodyne |
| | F-theta lens | 55-S96-16T | Custom design (built by Special Optics) |

**Supplementary Table 1** (continued)

| Module | Component | Product(s) | Manufacturer |
|---|---|---|---|
| Illumination sub-systems (four modules) | Illumination tube lens | 49-3630INK VIS-NIR coated achromatic lens | Edmund Optics |
| | Dichroic beam splitter | zt488/561rpc<br>zt488/594rpc | Chroma |
| Detection sub-systems (four modules) | Detection filter wheel | 96A354 filter wheel<br>MAC6000 DC servo controller | Ludl |
| | | RazorEdge and EdgeBasic long-pass filters: 488, 515, 561, 594 nm<br>BrightLine band-pass filters: 525/50 nm | Semrock |
| | Detection tube lens | 55-S240-16T | Custom design (built by Special Optics) |
| | Camera | Orca Flash 4.0 v2 camera<br>JULABO water chiller | Hamamatsu |
| Illumination and detection objectives (four modules) | Piezo objective positioner | P-622.1CD or P-628.1CD PIHera piezo linear stage<br>E-709.CHG digital controller | Physik Instrumente |
| | Objective base stage and flexure mount system | Aluminum flexure, stainless steel base with integrated spring mechanisms and micrometers | Custom design |
| | Objective | 54-23-15 | Custom design (built by Special Optics) |
| Specimen chamber | Four-view specimen chamber | Chamber manufactured from black Delrin<br>Bluestar 4370 silicone seals | Custom design |
| | Specimen holder | Plastic sample holder cup<br>Cup holder manufactured from medical-grade stainless steel<br>Adapter for multi-stage positioning system | Custom design |
| Specimen positioning system | Translation stages (3×) | M-111K046 | Physik Instrumente |
| | Rotary stage | M-116.2DG | Physik Instrumente |

**Supplementary Table 1** (continued)

| Module | Component | Product(s) | Manufacturer |
|---|---|---|---|
| Specimen positioning system | Motion controller | C-884.4D motion controller for DC servo motors | Physik Instrumente |
| FPGAs and electronic interfaces | PXI bus extender | PXIe/PCIe-8381 controller for PXI/PXIe modules<br>PXI-1065 chassis | National Instruments |
| | FPGAs | PXI-7853R multifunction reconfigurable I/O module<br>PXI-7842R multifunction reconfigurable I/O modules (3×) | National Instruments |
| | I/O interfaces | CB-68LPR connector blocks (4×)<br>SHC68-68-RMIO cables (4×)<br>CA-1000 enclosures (3×) | National Instruments |
| | Serial interface board | PXI-8430/4 | National Instruments |
| Control software | FPGA and host software modules | 64-bit LabVIEW code | Custom software |
| Microscope control workstation and image server | CXT9400 4U rackmount IsoView control and data acquisition workstation | Intel Xeon E5-2687WV2 CPUs (2×)<br>16 GB DDR-3 RAM modules (24×)<br>24-channel Adaptec 72405 RAID controllers (2×)<br>Samsung 840 Pro 512GB SSDs (2×)<br>Samsung 840 EVO 1TB SSDs (22×)<br>Firebird CameraLink frame grabber (4×)<br>Adaptec AFM-700 battery backup (2×)<br>Intel X520-SR1 SFP+ SR LC fiber network adapter<br>PNY nVidia Quadro K2000D graphics card | Colfax International |

**Supplementary Table 1** (continued)

| Module | Component | Product(s) | Manufacturer |
|---|---|---|---|
| Microscope control workstation and image server | CX4160s-XS6-JBOD 4U rackmount storage server | SuperMicro SuperStorage Server 5048R-E1CR36L platform<br>Intel Xeon E5-2630V3 CPU<br>16 GB DDR-4 RAM modules (8×)<br>LSI 9361-8i 8-channel RAID controller<br>Intel DC S3700 Series 200GB SSDs (2×)<br>Seagate Constellation ES.4 6TB hard disks (36×)<br>LSI LSICVM02 cache vault kit<br>Intel X520-SR1 SFP+ SR LC fiber network adapter | Colfax International |

**Supplementary Table 2 |** Specifications of IsoView imaging experiments

| Experiment | *Drosophila* functional imaging #1<br>elav-Gal4, 10×UAS-GCaMP6s | *Drosophila* developmental imaging<br>His2Av-mRFP1, spider-GFP |
|---|---|---|
| Related figures | Figs. 2a+b, 3; Suppl. Fig. 12 | Figs. 5, 6; Suppl. Figs. 14, 15 |
| Related videos | Video 2 | Video 6, 7 |
| Imaging mode | Simultaneous four-view imaging<br>Staggered confocal line detection | Simultaneous two-color imaging<br>Staggered confocal line detection |
| Excitation wavelengths | 488 nm | 594 nm and 488 nm |
| Illumination filters | ND 1.0 | |
| Objectives | Special Optics 54-23-15 custom objectives, $f$ = 15 mm, NA = 0.714 (water) | |
| Detection filters | BP525/50 | BP624/40 and BP525/50 |
| Cameras | Hamamatsu Orca Flash 4.0 v2 sCMOS (2048 × 2048 pixels) | |
| Temperature | 21.1°C | |
| Sample embedding | 1.2% low-melting temperature agarose in tap water | |
| Imaging period | 2 hours<br>7,205 time points | 3 hours<br>2,701 time points |
| Temporal sampling | 1 Hz | 0.25 Hz |
| Recording period per time point | 818 milliseconds | 3.15 seconds |
| Size of confocal detection window | 72 pixels (0.7 milliseconds) | |
| Staggered phase offset in orthogonal imaging arms | 200 pixels (1.95 milliseconds) | |
| Light-sheet sweep time | 18.05 milliseconds | |
| Camera exposure time | 18.05 milliseconds | |
| Average laser power | 70 µW | 139 µW (594 nm), 56 µW (488 nm) |
| Laser energy per image | 1.26 µJ | 2.51 µJ (594 nm), 1.01 µJ (488 nm) |
| Images per time point | 4 × 38 | 8 × 75 |
| Total # of images | 1,095,160 | 1,620,600 |
| Size of data set | 2.8 terabytes | 4.2 terabytes |
| Post-acquisition fusion and deconvolution | Content-based image registration<br>LR deconvolution (40 iterations) | Image registration in Fiji<br>LR deconvolution (40 iterations) |

**Supplementary Table 2** (continued)

| Experiment | *Drosophila* functional imaging #2 elav-Gal4 10×UAS-GCaMP6s | *Drosophila* functional imaging #3 elav-Gal4 10×UAS-GCaMP6s | *Drosophila* functional imaging #4 elav-Gal4 10×UAS-GCaMP6s |
|---|---|---|---|
| Related figures | Fig. 3; Suppl. Fig. 12 | Fig. 2c | Suppl. Fig. 13 |
| Related videos | - | Video 4 | Video 3 |
| Imaging mode | Sequential four-view imaging (alternating illumination and detection) | | |
| Excitation wavelengths | 488 nm | | |
| Illumination filters | BP488/10 | ND 1.0 | ND 1.0 |
| Objectives | Special Optics 54-23-15 custom objectives, $f$ = 15 mm, NA = 0.714 (water) | | |
| Detection filters | BP525/50 | | |
| Cameras | Hamamatsu Orca Flash 4.0 v2 sCMOS (2048 × 2048 pixels) | | |
| Temperature | 21.1°C | | |
| Sample embedding | 1.2% low-melting temperature agarose in tap water | | |
| Imaging period | 30 minutes<br>3,601 time points | 9 one-hour sessions (each session: 30 minutes imaging + 30 minutes break)<br>32,409 time points | 8 one-hour sessions (each session: 30 minutes imaging + 30 minutes break)<br>28,808 time points |
| Temporal sampling | 2 Hz | | |
| Recording period per time point | 492 milliseconds | 486 milliseconds | 495.2 milliseconds |
| Light-sheet sweep time | 1.0 millisecond | | |
| Camera exposure time | 3.9 milliseconds | 4.6 milliseconds | 4.6 milliseconds |
| Average laser power | 4.55 mW | 548 µW | 395 µW |
| Laser energy per image | 4.55 µJ | 0.55 µJ | 0.40 µJ |
| Images per time point | 4 × 40 | 4 × 35 | 4 × 36 |
| Total # of images | 576,160 | 4,537,260 | 4,148,352 |
| Size of data set | 831 gigabytes | 8.7 terabytes | 9.5 terabytes |
| Post-acquisition fusion and deconvolution | Content-based image registration<br>Lucy-Richardson (LR) deconvolution (40 iterations) | | |

**Supplementary Table 2** (continued)

| | |
|---|---|
| Experiment | Zebrafish functional imaging<br>HuC::H2B-GCaMP6s |
| Related figures | Fig. 4 |
| Related videos | Video 5 |
| Imaging mode | Sequential four-view imaging<br>(alternating illumination and detection) |
| Excitation wavelengths | 488 nm |
| Illumination filters | ND 1.0 |
| Objectives | Special Optics 54-23-15 custom objectives<br>$f$ = 15 mm, NA = 0.714 (water) |
| Detection filters | BP525/50 |
| Cameras | Hamamatsu Orca Flash 4.0 v2 sCMOS<br>(2048 × 2048 pixels) |
| Temperature | 21.1°C |
| Sample embedding | 1.0% low-melting temperature agarose in tap water |
| Imaging period | 24 minutes<br>1,450 time points |
| Temporal sampling | 1 Hz |
| Recording period per time point | 999.8 milliseconds |
| Light-sheet sweep time | 1.0 millisecond |
| Camera exposure time | 5.7 milliseconds |
| Average laser power | 564 μW |
| Laser energy per image | 0.56 μJ |
| Images per time point | 4 × 67 |
| Total # of images | 388,600 |
| Size of data set | 1.4 terabytes |
| Post-acquisition fusion and deconvolution | Content-based image registration<br>Lucy-Richardson (LR) deconvolution (40 iterations) |

**Supplementary Note |** IsoView light-sheet microscope alignment

The following steps outline the alignment procedure for the IsoView microscope.

Step 1: The relay lenses, f-theta lenses, illumination tube lenses, and dichroic beam splitters are mounted on XY-adjustable mounts and adjusted such that the laser beams are transmitted on-axis along the rails in the four illumination paths.

Step 2: The objectives are adjusted using the custom objective base stage and flexure mount system. The custom bases allow transverse-axial translation and yaw rotation and the custom flexures allow vertical translation of the objectives for on-axis transmission of the laser beams across opposing illumination rails. At the conclusion of these adjustments, the opposing illumination beams overlap with one another and the beams from orthogonal arms intersect at a right angle in sample space.

Step 3: The detection tube lenses, mounted on XY-adjustable lens mounts, are adjusted such that the illumination beams from the opposing rails are transmitted on-axis along the rails in the detection paths.

Step 4: Next, a thin glass micro-needle tip, about 5-10 μm in diameter, is positioned at the intersection of the illumination beams in the sample chamber. With the objective piezo positioners at the center of their travel range, the custom objective bases are translated axially until the needle tip appears in focus on all four cameras. The lateral position and the yaw are adjusted to have the needle tip appear centered in each camera's field of view (FOV) and also in focus as the needle is translated laterally across each camera's FOV. Thus, the opposing detection planes are now overlapping, the orthogonal detection planes are intersecting at the center of each camera's FOV, and the detection planes are coplanar with the illumination beams from the orthogonal arms.

Step 5: Although the opposing illumination beams are now overlapping and coplanar with the detection planes of the orthogonal cameras, the thinnest portions of the weakly-focused illumination beams are not necessarily centered on these cameras' FOVs. To correct for possible mismatches in this respect, an alignment mirror is positioned in the sample plane and rotated to a 45° angle between each pair of orthogonal objectives, and the light-sheet profiles are subsequently mapped across each FOV. The illumination tube lens positions are then adjusted in the direction of beam propagation to have the thinnest portion of the light sheets be centered on the cameras' FOVs. Also, if light-sheet profiles are slightly converging or diverging across the cameras' FOVs,

these alignment imperfections are corrected by adjusting the relative positions of f-theta lenses and dual-axis galvanometer scanners.

Step 6: The alignment procedure is complete once the opposing detection planes overlap, are coplanar with opposing light sheets that have their thinnest portions centered on the cameras' FOVs, and are intersecting the orthogonal detection planes at the center of the associated FOVs. If there is any residual yaw in light sheets relative to detection planes, this can be corrected by shifting the beam exiting the galvanometer scanner laterally, which can be achieved by moving the dual-axis galvanometer scanner sideways relative to the propagation direction to the exit beam. Similarly, any residual offset between the lateral positions of the two opposing light sheets and the detection planes can be fine-tuned using the lateral-adjustment mirror of the dual-axis scanner.